PAPER

Homogeneous percolation *versus* arrested phase separation in attractively-driven nanoemulsion colloidal gels†

Matthew E. Helgeson,*[a] Yongxiang Gao,[a] Shannon E. Moran,[b] Jinkee Lee,[c] Michael Godfrin,[d] Anubhav Tripathi,[d] Arijit Bose[e] and Patrick S. Doyle[b]

We elucidate mechanisms for colloidal gelation of attractive nanoemulsions depending on the volume fraction (ϕ) of the colloid. Combining detailed neutron scattering, cryo-transmission electron microscopy and rheological measurements, we demonstrate that gelation proceeds by either of two distinct pathways. For ϕ sufficiently lower than 0.23, gels exhibit homogeneous fractal microstructure, with a broad gel transition resulting from the formation and subsequent percolation of droplet–droplet clusters. In these cases, the gel point measured by rheology corresponds precisely to arrest of the fractal microstructure, and the nonlinear rheology of the gel is characterized by a single yielding process. By contrast, gelation for ϕ sufficiently higher than 0.23 is characterized by an abrupt transition from dispersed droplets to dense clusters with significant long-range correlations well-described by a model for phase separation. The latter phenomenon manifests itself as micron-scale "pores" within the droplet network, and the nonlinear rheology is characterized by a broad yielding transition. Our studies reinforce the similarity of nanoemulsions to solid particulates, and identify important qualitative differences between the microstructure and viscoelastic properties of colloidal gels formed by homogeneous percolation and those formed by phase separation.

Introduction

Colloidal gels are sample-spanning networks formed from attractively-driven chains and clusters of particles.[1] Due to their unique structural and mechanical properties, they hold important applications in various fields, ranging from formulation of foods,[2] paints, drilling fluids, templates for porous materials[3] and advanced inks designed for 3D printing.[4] Colloidal gels also serve as model systems for studying arrested states in attractive fluids, due to their experimentally observable microstructure relative to molecular systems.[5]

Despite this widespread utility, the fundamental mechanisms of colloidal gelation are still under debate, particularly at

[a]Department of Chemical Engineering, University of California Santa Barbara, Santa Barbara, CA 93117, USA. E-mail: helgeson@engineering.ucsb.edu; Fax: +1 805 893 4731; Tel: +1 805 893 3372

[b]Department of Chemical Engineering, Massachusetts Institute of Technology, Cambridge, MA 02139, USA

[c]School of Mechanical Engineering, Sungkyunkwan University, Suwon, Gyeonggi-do 440-746, Korea

[d]School of Engineering, Brown University, Providence, RI 02912, USA

[e]Department of Chemical Engineering, University of Rhode Island, Kingston, RI 02881, USA

moderate particle volume fraction (ϕ). For example, in systems with very short-range (near-contact) attractions, Eberle *et al.* recently proposed that gelation arises from homogeneous percolation,[6,7] whereby attractively-driven clusters reach sample-spanning dimensions, based on the observation that the experimentally observed gelation boundary follows closely to the theoretical predicted dynamic percolation line.[8] By contrast, previous studies on systems with short-range, non-contact attractions induced by polymer depletion have found that colloidal gelation occurs directly at the gas–liquid spinodal boundary.[9,10] As such, many studies have proposed[9–14] that gelation results from arrested phase instability: the system spontaneously phase separates into colloid-rich and colloid-poor regions and the process becomes arrested due to an attractive glass transition in the colloid-rich region.[1] Elucidating which of these mechanisms leads to gelation in an attractive system is not only of fundamental scientific interest,[1,15,16] but also of practical importance, because different mechanisms imply distinct kinetics that can be used to control the structure and mechanical properties of colloidal gels.

Moreover, the process of yielding and flow in colloidal gels is critical in their processing and applications, and has received significant recent interest.[17] Whereas dilute gels typically exhibit a distinct yield stress (or strain) in nonlinear rheological measurements[18] corresponding to a single microstructural process,[19] more concentrated systems exhibit complicated

yielding in which the transition from solid-like behaviour to flow is marked by a two-step or broadened transition.[20–23] Such two-step yielding has been primarily observed in systems with moderate volume fraction, and has been hypothesized to occur due to a combination of processes, including rupture of interparticle bonds and glassy dynamics of attractive clusters.[22,24] However, it is unclear how such a mechanism depends on the quiescent microstructure of the gel and, ultimately, the mechanism of gelation.

Recently, we have discovered the thermoreversible formation of colloidal gels in complex oil-in-water (O/W) nanoemulsions containing temperature-sensitive end-functionalized polymers in the continuous phase.[25,26] In these systems, interdroplet attractions are hypothesized to occur from polymer bridging, and can be dynamically and reversibly modified through small changes in temperature in order to drive colloidal gelation of the droplet phase. As such, these systems provide an excellent platform for studying the mechanisms and kinetic pathways of colloidal gelation, as the system can be observed under quasi-equilibrium conditions en route to gelation, allowing characterization of the pristine gelled state. Such studies could also better elucidate the behaviour of irreversible nanoemulsion gels,[27] whose structure and rheology strongly resembles their hard particle counterparts.

In this work, we use thermosensitive nanoemulsions in order to carefully monitor the microstructure and rheology of colloidal gels throughout the gelation process. In particular, we perform studies on a range of droplet volume fraction spanning the dilute regime to more concentrated suspensions above the predicted critical point for adhesive hard spheres ($\phi_c \sim 0.26$). Combining measurements including rheology, small and ultra-small angle neutron scattering (SANS/USANS), and direct visualization by cryo-TEM allows detailed interrogation of the kinetic mechanisms of gelation.

Results

Rheology

Thermal rheology of the O/W nanoemulsions indicates thermoreversible gelation over the entire range of concentrations studied ($\phi = 0.12$–0.33). Although thermal gelation was previously observed below $\phi = 0.12$,[25] the associated rheological transitions were not observed here due to insufficient increases in moduli and prohibitively high gel temperatures.

The gelation process can most easily be seen in temperature ramp experiments under small-amplitude oscillatory shear (Fig. 1a).[25] At sufficiently low temperatures, the viscous modulus (G'') exceeds the elastic modulus (G') for all applied frequencies, corresponding to liquid-like behaviour. However, at a certain temperature (T_1), G' and G'' increase abruptly by several orders of magnitude. At an intermediate temperature (T_2), G' exceeds G'', indicating the formation of a solid-like network within the fluid. At high temperatures, the moduli reach a plateau that is approximately independent of temperature.

Interestingly, we find two distinct types of rheological behaviour depending on the droplet volume fraction. Representative samples of the thermal rheology, including small and

large-amplitude oscillatory viscoelasticity, exhibiting these two different characteristic behaviours are shown in Fig. 1a. For $\phi < 0.23$ (Fig. 1a, top), the observed gel transition is very broad, with the increase in moduli spanning a temperature range of 10–15 °C. By contrast, for $\phi > 0.23$ (Fig. 1a, bottom), gelation is significantly more abrupt, with the entire transition occurring over as few as 3 °C.[25]

The gel point

Numerous methods have been identified to determine the gel point of colloidal gels, including simple tube inversion,[11] dynamic light scattering,[28] conductivity,[29] and small-amplitude rheological measurements.[30] Here, we choose to quantify the gelation temperature(s) directly from the temperature ramp rheological data (Fig. 1, top) to facilitate comparison with the microstructural measurements to follow (this will be validated later). An initial gel temperature, T_1, is defined by the temperature at which G' initially begins to increase from its low-temperature value. Quantitatively, T_1 was determined by determining the asymptotic intersection of linear and power-law fits of the low and high-temperature data, respectively. In cases where G' was immeasurable at low temperatures, T_1 was chosen as the temperature at which G' was first observed. Subsequently, we define a critical gel temperature, T_2, as the temperature at which G' and G'' are equal, following the criterion for critical gelation suggested by Winter and Chambon,[30] where $G'(\omega) = G''(\omega) \sim \omega^\alpha$ at the gel point, where α is related to the universality class of the percolation transition. The qualitative differences in the gelation transition between the low-ϕ and high-ϕ regimes are reflected in the differences between T_1 and T_2 with increasing ϕ (Fig. 1c). For $\phi < 0.23$, T_1 and T_2 differ significantly, representing a broad gel transition, whereas for $\phi > 0.23$, T_1 and T_2 differ by only a few degrees. In the former case, we find that samples equilibrated at temperatures corresponding to $T_1 < T < T_2$ are stable for several hours, and exhibit viscoelasticity that is intermediate between the fluid and gelled state (see ESI†). Furthermore, we note that the dependence of T_2 on ϕ changes abruptly near $\phi = 0.23$.

Linear viscoelasticity

The difference between the two concentration regimes of gelation is further evident by changes in linear viscoelasticity through the gel transition. In particular, $\phi = 0.21$ and $\phi = 0.33$ were selected as characteristic compositions in the low-ϕ and high-ϕ regimes, respectively, for which frequency sweeps were performed at temperatures spanning the gel transition (Fig. 1b). In both cases, the linear viscoelasticity at temperatures well below T_1 (green symbols) exhibits scaling of $G' \sim \omega^2$ and $G'' \sim \omega^1$, indicating liquid-like behaviour. At temperatures between T_1 and T_2, in both the low-ϕ and high-ϕ regimes, the moduli approach scalings of $G' \approx G'' \sim \omega^{1/2}$, indicating approach to the critical gel point. The scaling exponent of $\alpha = 1/2$ has been observed previously for both chemically gelling polymers[30] and physically gelling near-hard sphere suspensions.[6,11] We note that the temperatures at which this behaviour occurs are in agreement with the values of T_2 obtained from temperature
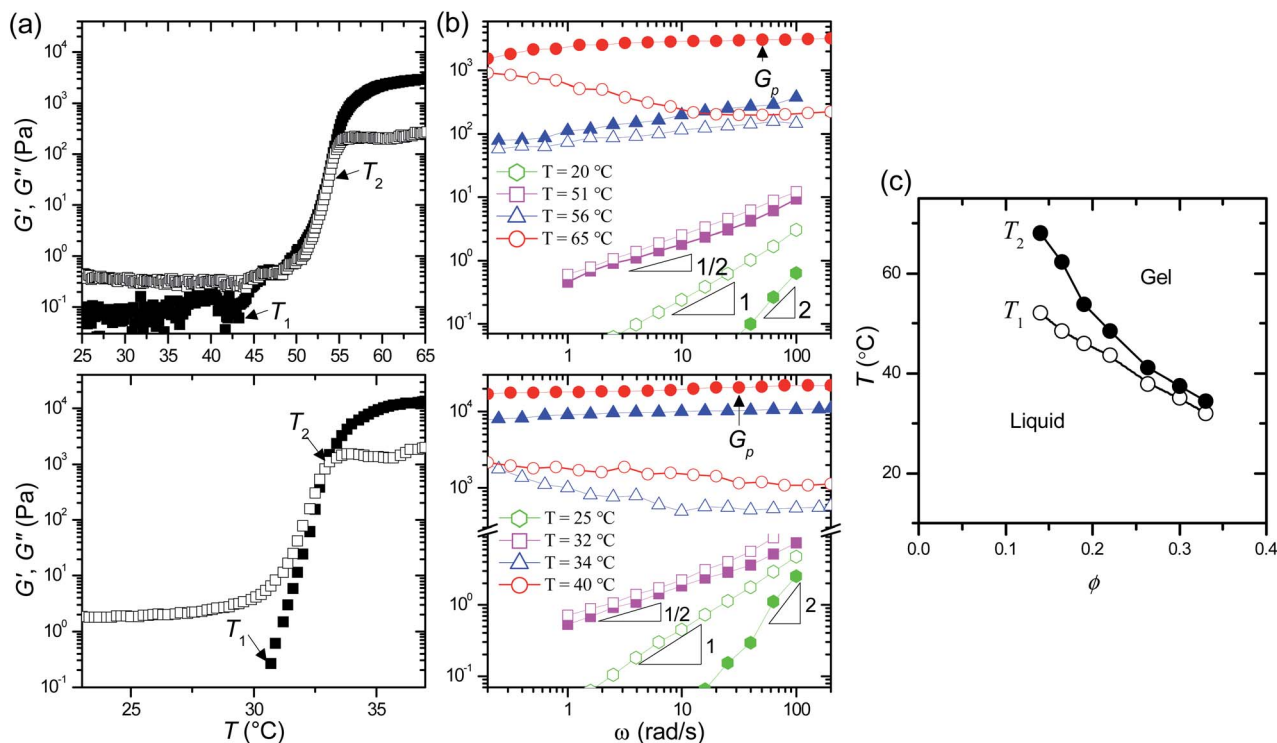
Fig. 1 Rheological characterization of nanoemulsions with $\langle a \rangle = 18$ nm containing (top) $\phi = 0.22$ and (bottom) $\phi = 0.33$. (a) Thermal scans of elastic modulus G' (closed symbols) and viscous modulus G'' (open symbols) versus temperature, indicating the apparent gel temperatures T_1 and T_2. (b) Frequency sweeps of G' and G'' versus oscillatory frequency for the temperatures indicated in the linear viscoelastic regime ($\gamma_0 = 0.05\%$). (c) Colloidal phase diagram for nanoemulsions containing droplets with $\langle a \rangle = 18$ nm. Points give the apparent gel temperatures corresponding to panel (a).

ramps, validating the procedure outlined above to determine the critical gel temperature.

Above T_2, significant differences in the evolution of linear viscoelasticity are observed. For $\phi = 0.21$ (Fig. 1b, top), the moduli show near-critical scaling for temperatures well above T_2 (blue points), suggesting that the incipient gel remains at the percolation threshold well into the gelation process. Eventually, once the high-temperature plateau is reached (red points), the linear viscoelasticity of the gel exhibits $G' > G''$ over the observable frequency window. However, significant frequency dependence is observed, with a minimum in G'' at moderate frequencies.

The sample with $\phi = 0.33$ shows significantly different behaviour (Fig. 1b, bottom). First, the near-critical scaling of the gel moduli disappears soon after T_2 (blue points), and is replaced with frequency-dependent behaviour similar to that observed in the low-ϕ regime at high temperatures. However, once the high-temperature plateau is reached, the moduli become nearly frequency-independent, although a weak minimum in G'' is still observed at similar frequencies to that observed in the low-ϕ sample.

In both the low-ϕ and high-ϕ regimes, the strength of the gel can be characterized by the plateau modulus, G_P, defined as the value of G' at the frequency corresponding to the minimum in G''. The dependence of G_P on volume fraction shows further evidence for two distinct regimes of gelation (Fig. 2a). At both

asymptotically small and large ϕ, a power-law scaling of $G_P \sim \phi^m$ is observed. However, the scaling exponents differ significantly between these limits ($m = 16.9$ and 2.9, respectively).

The frequency-dependence of the linear viscoelasticity of our nanoemulsion gels has also been reported for polymer depletion-induced colloidal gels[11] and dense emulsions,[27] and is well-understood in terms of glassy dynamics.[31] For attractive systems, the glassy state is often depicted as the trapping of particles (or particle clusters) within a "cage" of attractive potential wells (or "bonds") between nearest neighbours. The short-time (β) relaxation thus represents fluctuations of structural elements within their local well, whereas the long-time (α) relaxation represents their escape from the well. In terms of linear viscoelasticity, a crossover between G' and G'' occurs at the characteristic rate of the α relaxation, whereas the minimum in G'' signifies a transition from α-dominated dissipation (related to the release of elastic constraints) to β-dominated dissipation (related to hydrodynamic modes).

Applying this framework to the present nanoemulsion gels, we surmise that the distinct differences in linear viscoelasticity between the low-ϕ and high-ϕ regimes at high temperatures arise from significant differences in the nature of the α-relaxation between the two regimes. One possible explanation for this is simply the volume fraction dependence of the glassy dynamics, which slow with increasing ϕ above the percolation threshold.[32] However, this is unlikely as the minimum in G'' is
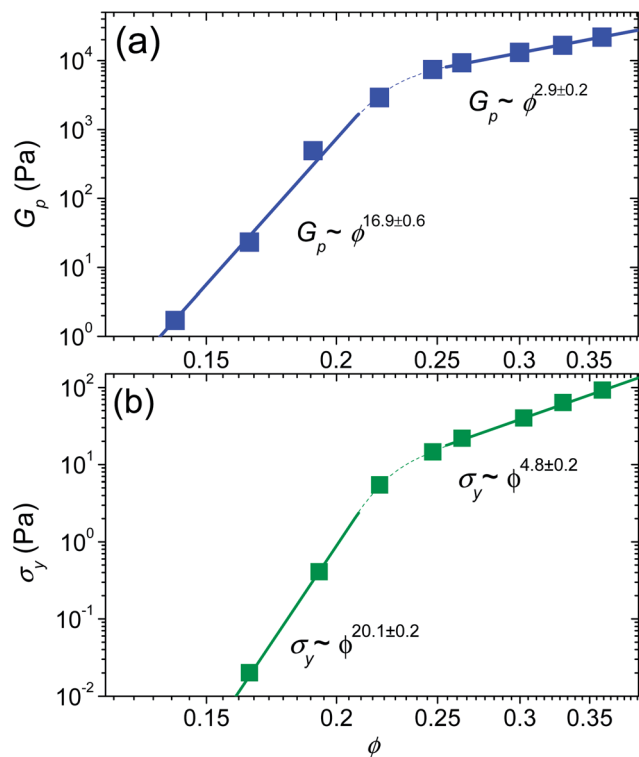
Fig. 2 Gel modulus (a) and apparent yield stress (b) for nanoemulsion gels *versus* droplet volume fraction, ϕ. Solid lines give asymptotic fits in the low-ϕ and high-ϕ regimes. Dotted lines are drawn to guide the eye.
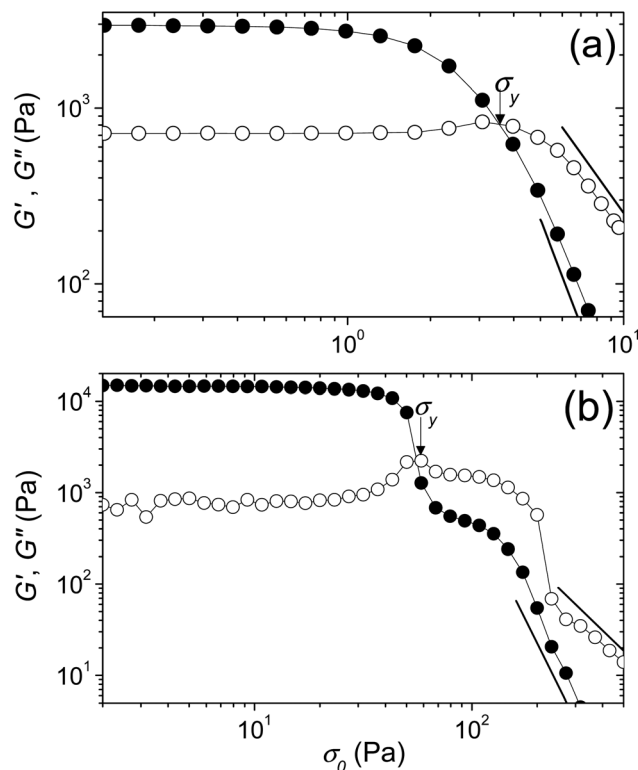

Fig. 3 Large amplitude oscillatory shear (LAOS) rheology of G' and G'' *versus* stress amplitude through the yielding transition, indicating the apparent yield stress for (a) $\phi = 0.21$ and (b) $\phi = 0.33$.

similar in both the low-ϕ and high-ϕ regimes. Another possible explanation is that the distribution of particle–particle or cluster–cluster bonds is significantly different between the two regimes. We will test these alternative explanations for the qualitatively different viscoelasticity in what follows.

Non-linear viscoelasticity and yielding

To further probe differences in the two concentration regimes, we performed large amplitude oscillatory stress (LAOS) measurements. Characteristic stress sweep data is shown for $\phi = 0.21$ and $\phi = 0.33$ in Fig. 3. For $\phi < 0.23$, the stress sweeps are qualitatively similar to hard particle gels under dilute conditions.[18,19] Specifically, at sufficiently high stress amplitude, σ_0, the material exhibits a single, relatively smooth yielding transition from a linear solid (where G' and G'' are independent of σ_0) to a shear-thinning liquid with power-law scaling of G' and G'' with increasing stress at high amplitudes (Fig. 3, solid lines). Here, yielding is characterized by a single yield stress, σ_y, where G' and G'' intersect and G'' shows a mild maximum with increasing σ_0.

By contrast, gels with $\phi > 0.23$ show significantly different yielding behaviour, where the transition between the linear and the fluid regime is significantly broader, bearing similarity to the so-called "two-step" yielding observed in a number of colloidal gels at intermediate ϕ.[17,21,23,24,33] Specifically, the maximum in G'' is more pronounced, although it still occurs at the initial yield stress. However, at higher σ_0, both G' and G'' exhibit a plateau over a significant range of stress. This plateau

persists until approximately 2–$3\sigma_0$, after which the fluid regime is finally obtained. Also, we note that some samples in this regime exhibit anomalous jumps in moduli during the transition to flow, which could potentially be the result of wall slip. However, we will leave detailed studies of the high-stress (or strain) behaviour for future investigations.

Since gels in both the low-ϕ and high-ϕ regimes exhibit a clear initial yield point, we compare the scaling of the yield stress, σ_y, with volume fraction between the two regimes (Fig. 2b). In both cases, we find asymptotic scaling of $\sigma_y \sim \phi^n$. However, as with the linear modulus, we find a significant difference between the two asymptotic limits ($n = 20.1$ and 4.8, respectively).

Neutron scattering

Our rheological measurements clearly establish the presence of two distinct regimes of gelation with significantly different asymptotic scaling of their viscoelasticity. To better understand their origins, we performed combined SANS and USANS measurements for the samples containing $\phi = 0.21$ and $\phi = 0.33$ at temperatures spanning the gel transition. Due to the thermoreversible nature of gelation in these systems,[25] this provides deep insight into the gelation process that would be difficult to obtain for many other systems. Furthermore, to our knowledge, the q-range these measurements represent (10^{-5} to 10^{-1} Å^{-1}), spanning the length scale of 1–10 000 droplets, is the most comprehensive to date for colloidal gels, including measurements

by neutron[7] and X-ray scattering,[34] light scattering,[35–37] optical microscopy,[14,38,39] and combinations thereof.[40]

Low-ϕ regime. Combined SANS/USANS spectra from the sample with $\phi = 0.21$ ($T_1 = 41$ °C, $T_2 = 48$ °C) at temperatures spanning the gel transition are shown in Fig. 4a. The results are plotted by subtracting the incoherent background intensity (determined by Porod analysis of the high-q data) from the measured scattering intensity, $I(q)$. Since the PEGDA polymer is contrast-matched, the quantity plotted thus represents the coherent scattering arising from the droplets only.
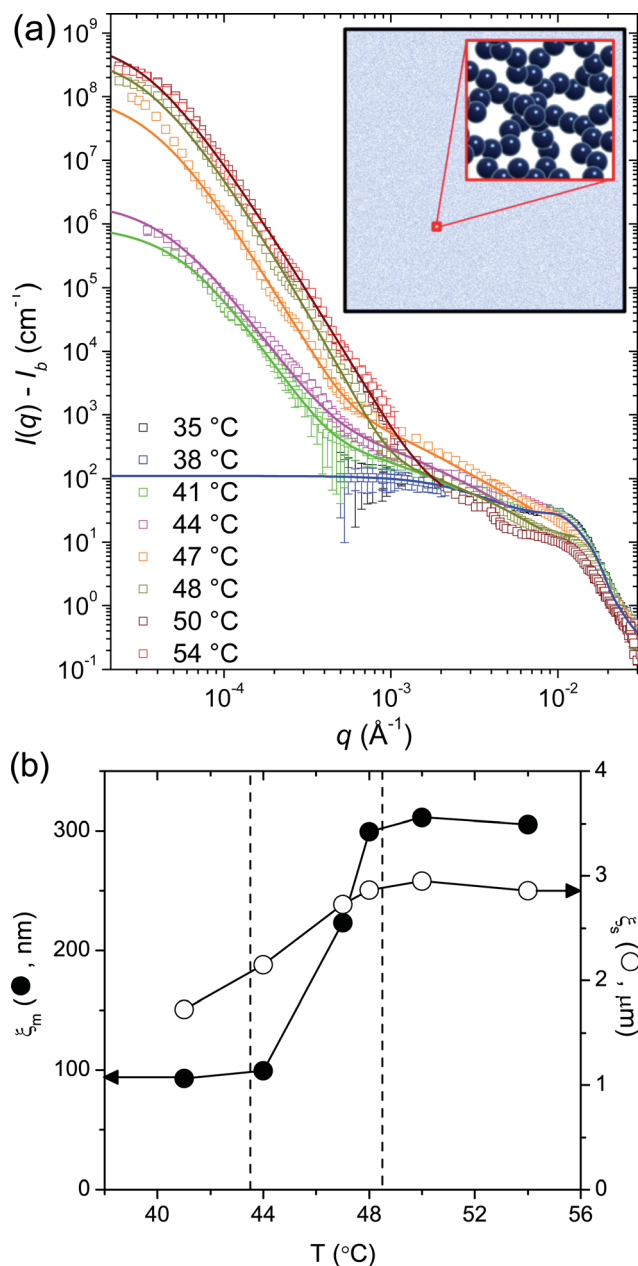

Fig. 4 (a) Combined SANS/USANS spectra of the coherent scattering, $I(q) - I_b$ *versus* the wave vector q, through the gel transition for $\phi = 0.21$ at temperatures indicated. Lines give fits to eqn (1). Inset shows the hypothesized homogeneous structure (porosity has been exaggerated for visual clarity). (b) Best-fit correlation lengths for the mass fractal (left axis) and surface fractal (right axis).

At temperatures below T_1, the nanoemulsion exhibits q-independent intensity at sufficiently low q-values, indicating liquid-like structure. To prove this, we fit the data at 38 °C to polydisperse spheres with square well interactions whose strength, ε, and range, δ, were fixed and set equal to those measured on dilute suspensions at a similar temperature in previous work (Table 1).[25] The resulting best fit (blue line, parameters in Table 1) is in quantitative agreement with the data. We further note that the high-q scattering ($q\langle D \rangle/2 > 2$) is unchanged over the entire temperature range, indicating that the droplets do not significantly change their size distribution over the course of measurement, as previously shown.[25]

At temperatures between T_1 and T_2, significant changes in the low-q scattering are observed. Specifically, two different power-law regimes of the coherent scattering emerge, one at $10^{-3} < q < 10^{-2}$, and one at $q < 10^{-3}$. Such power-law behaviour is characteristic of fractal structures.[41,42] At even lower q-values, the coherent scattering exhibits a plateau, indicating a finite characteristic size of structural features. As gelation proceeds (*i.e.* the temperature is increased from T_1 to above T_2), the excess low-q scattering increases dramatically, indicating the presence of strong density correlations in the system. Ultimately, at temperatures above T_2, the scattering saturates, indicating that the structure becomes arrested at the critical gel point. As noted above, the rheology of various intermediate states is stable over the time period of measurement for both SANS and USANS, and so the scattering can be viewed as coming from quasi-equilibrium structures at various intermediate points along the gel transition.

This scattering is reminiscent of that observed in dilute colloidal gels ($\phi = 0.02$–0.08) of monodisperse spheres in the absence of polymer.[40] Using these previous studies as a guide, we fit the data in Fig. 4 to a phenomenological model for mass fractal objects (with mass fractal dimension d_m and correlation length ξ_m) enclosed by a surface fractal (with surface fractal dimension d_s and correlation length ξ_s)[43]

$$I(q) - I_b = \frac{K_1 \sin[(d_m - 1)\mathrm{atan}(\xi_m q)]}{(d_m - 1)(\xi_m q)\left[1 + (\xi_m q)^2\right]^{\frac{d_m - 1}{2}}}$$
$$+ \frac{K_2 \sin[(d_m - d_s - 1)\mathrm{atan}(\xi_s q)]}{(\xi_s q)\left[1 + (\xi_s q)^2\right]^{\frac{d_m - d_s + 2}{2}}} \quad (1)$$

where K_1 and K_2 set the relative contributions of the mass and surface fractal, respectively, to the overall scattering. We note that eqn (1) ignores the high-q portion of the structure (*i.e.* droplet morphology and local droplet–droplet interactions),

Table 1 Best-fit SANS/USANS model parameters for $T < T_1$

Parameter	Value
Average diameter, $\langle D \rangle$	34.8 nm
Polydispersity, $\sigma/\langle D \rangle$	0.375
Scattering length density contrast, $\Delta\rho$	3.973×10^{-7} Å^{-2}
Square well width, $\lambda/\langle D \rangle$	0.068
Square well depth, $\varepsilon/k_B T$	0.117

and furthermore assumes that the mass and surface fractals are uncorrelated, which is only strictly true in the limit $\xi_m \ll \xi_s$.

The data at all temperatures above T_1 are well-fit by the model (Fig. 4a, lines). From this, we hypothesize that the gel microstructure in the low-ϕ regime consists of a homogeneous network of fractal-like droplet clusters (Fig. 4a, inset). Table 2 shows the resulting best-fit model parameters. Interestingly, we find that $d_m \sim 1.6$ is nearly constant throughout the entire gel transition. We note that care must be taken in comparing this apparent mass fractal dimension to theories, as the high-q scattering contains a significant contribution from the local, non-fractal structure of the clusters on the order of the droplet size. Wu *et al.* performed Monte Carlo simulations on dispersions of monodisperse attractive spheres to account for this, and found that gels with an apparent $d_m \sim 1.7$ from SANS measurements had a "true" fractal dimension of 2.35.[40] Assuming similar effects in our data, we surmise that the droplets form fairly dense clusters, with a characteristic length scale (ξ_m) that grows from several droplets at T_1 to tens of droplets at T_2 (Fig. 4b).

We note that the surface fractal contribution to the scattering is present over the entire gel transition, where d_s decreases mildly with an associated length scale (ξ_s) on the order of several microns (Fig. 4b). Since the criterion for uncorrelated mass and surface fractals ($\xi_m \ll \xi_s$) is not satisfied, it is unclear exactly what the surface fractal contribution arises from aside from the natural surface of the mass fractal itself. One possibility is that the finite size of mass fractal clusters at percolation (signified by the low-q plateau) is due to the formation of multiple clusters within the scattering volume at T_1, which then jam at T_2 resulting in macroscopic gelation. In this scenario, the surface fractal contribution to the scattering could represent grain-like boundaries or voids between jammed clusters. This is also consistent with the relatively large values of K_2 relative to K_1, which signify large-amplitude density variations between the clusters and interstitial voids. However, we stress that this is merely a hypothesis, and the true origin of the surface fractal scattering remains unclear.

High-ϕ regime. SANS/USANS measurements on the sample with $\phi = 0.33$ (Fig. 5a) exhibit liquid-like suspension microstructure at temperatures below T_1, which again is well-described by a suspension of polydisperse spheres with square-well interactions (blue line). As for the lower volume fraction, a significant and sudden excess low-q scattering is observed at T_1, which at intermediate q-values exhibits power-law scaling indicative of fractal microstructure.

The scattering for $\phi = 0.33$ through the gel transition exhibits several qualitative differences compared to the low-ϕ regime. The most important is the appearance of a significant peak at very low q-values ($q < 10^{-4}$ Å^{-1}), signifying strong structural correlations at length scales orders of magnitude larger than the droplet size. Remarkably, the entire structural transition occurs over 0.5 °C, with the scattered intensity saturating above 31 °C. We also note that the scattering spectra are identical at q-values above the peak, and exhibit power-law behaviour similar to what was observed at low ϕ, suggesting a similar fractal-like structure at intermediate length scales that

Table 2 Best-fit model parameters for the combined mass/surface fractal model for $\phi = 0.21$

T (°C)	K_1 (cm^{-1})	d_m	ξ_m (nm)	K_2 (cm^{-1})	d_s	ξ_s (nm)
41	254	1.60	92.9	4.66×10^5	1.62	1720
44	386	1.58	99.6	1.18×10^6	1.70	2150
47	1950	1.57	223	5.64×10^7	1.52	2720
48	1970	1.59	299	2.36×10^8	1.54	2870
50	1150	1.52	311	4.16×10^8	1.50	2950
54	1150	1.53	306	3.52×10^8	1.50	2860

persists as the large-scale density correlations grow. The significantly steeper power-law slope in this region ($q^{-2.7}$) is close to what would be expected for close-packed spheres.[44] The persistence of the mass fractal scattering to q-values close to q_{max} suggests that the fractal clusters grow self-similarly as gelation proceeds, unlike the low-ϕ case where the fractal scaling changes continually throughout the gel transition.

The appearance of a significant low-q peak in light scattering measurements has been previously observed during gelation of attractive particulate suspensions.[35,36,39,45] However, there remains some debate as to the origin of the peak. Some authors have proposed that the peak represents a limiting cluster size, above which effective cluster repulsions (possibly due to excluded volume effects) give rise to the observed cluster–cluster correlations.[36] Alternatively, others have proposed that the low-q peak signifies a large-scale structure with correlated heterogeneity reminiscent of microphase separation.[39,45] In this case, the strong cluster–cluster correlations arise from a tight distribution of characteristic lengths between cluster-rich and cluster-poor domains within the material.

We fit the data to a novel model that combines the intermediate-q mass fractal behaviour observed in the low-ϕ gel with an additional low-q contribution due to phase separation. For the latter, we use an expression derived previously from a normal mode analysis of the linearized Cahn–Hilliard equation,[46]

$$I(q) - I_b = \frac{K_1 \sin\left[(d_m - 1)\mathrm{atan}(\xi_m q)\right]}{(d_m - 1)(\xi_m q)\left[1 + (\xi_m q)^2\right]^{\frac{d_m - 1}{2}}}$$
$$+ \frac{K_2 \left[\dfrac{\xi_c}{1 + (q - \beta_{max})^2 \xi_c^2} - \dfrac{\xi_c}{1 + (q + \beta_{max})^2 \xi_c^2}\right]}{(\beta_{max} q)}. \quad (2)$$

The first term corresponds to homogeneous mass fractal clusters with dimension d_m and characteristic size ξ_m, and the second term corresponds to density correlations associated with the fastest growing unstable mode of the phase separation, with wavelength β_{max}. The two-Lorentzian form of the latter arises due to an exponentially limiting cutoff size, ξ_c, assumed for long-wavelength correlations in order to capture experimentally-observed behavior.[47] The model quantitatively captures both the sharpness of the peak (expressed by the product $\xi_c \beta_{max}$) as well as the intermediate-q scattering for $T > T_1$. The poor fit of the peak at the temperature just below T_1
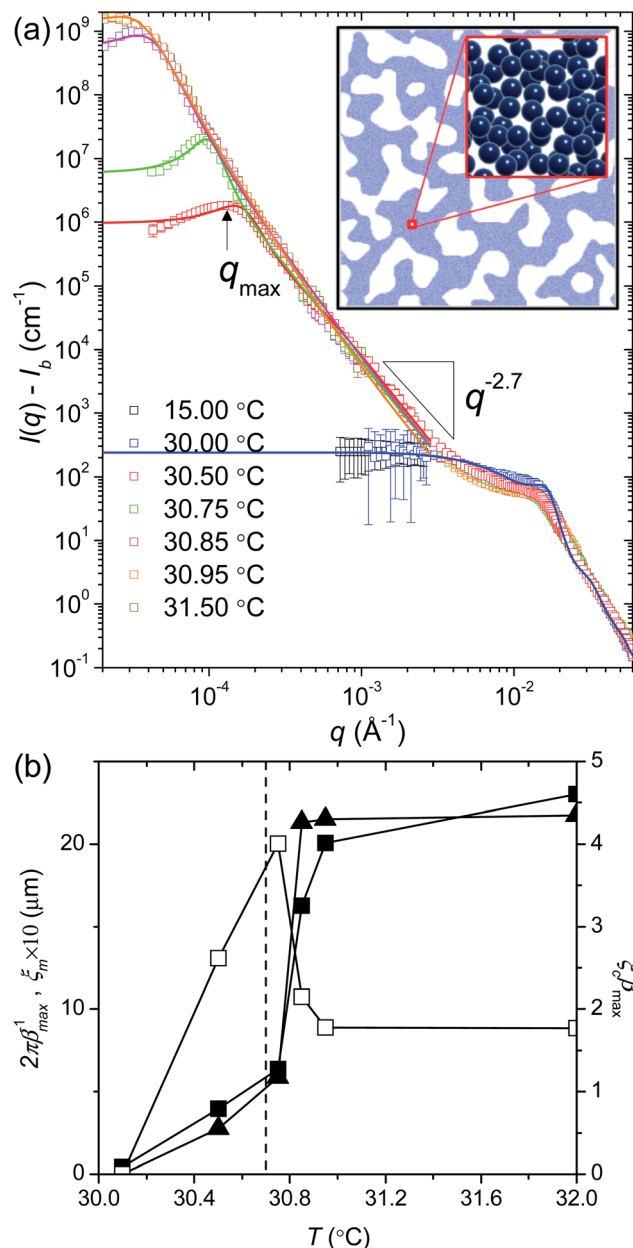
Table 3 Best-fit model parameters for the combined mass fractal/phase separation model for $\phi = 0.33$

T (°C)	K_1 (cm^{-1})	d_m	ξ_m (μm)	K_2 (cm^{-1})	β_{max} (μm^{-1})	ξ_c (μm)
30.00	—	—	—	—	—	—
30.50	2.40×10^5	2.70	0.274	2.45×10^6	1.58	1.65
30.75	1.75×10^6	2.70	0.587	4.55×10^6	0.987	4.06
30.85	3.41×10^7	2.70	2.13	2.29×10^7	0.386	5.57
30.95	4.39×10^7	2.70	2.15	2.84×10^7	0.313	5.69
31.50	4.42×10^7	2.70	2.17	2.46×10^6	0.274	6.46

the order of microns. Interestingly, we find that the scattering peak is sharpest ($\xi_c\beta_{max}$ is largest) at T_1, suggesting that the density correlations due to phase separation are most uniform precisely at the gel point. This is consistent with previous reports on depletion-induced hard particle gels at similar volume fraction,[11] which found that density correlations were strongest in the vicinity of the gel point, although the associated correlation peak was not directly observed. These results provide strong evidence that gelation in the high-ϕ regime is caused by arrested phase separation.

Cryo-TEM

Cryo-TEM measurements of the gelling samples at $\phi = 0.21$ and 0.33 were performed at several temperatures spanning the gel transition (Fig. 6). Images taken of samples vitrified at 25 °C (significantly below T_1 for both samples) exhibit similar features. Specifically, the suspension appears as predominantly dispersed droplets with diameters of 30–40 nm, consistent with the droplet size measured by DLS. Among the well-dispersed
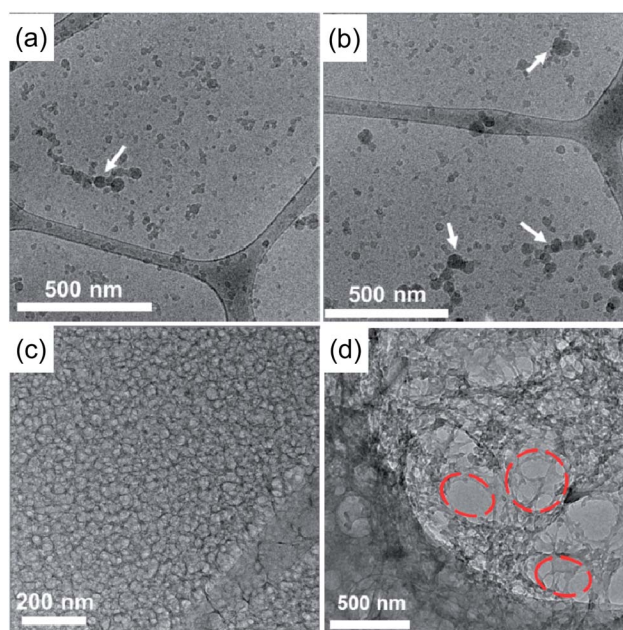
Fig. 5 (a) Combined SANS/USANS spectra of the coherent scattered intensity, $I(q) - I_b$, versus the wave vector q through the gel transition for $\phi = 0.33$ at temperatures indicated. Lines give fits to eqn (2). Inset shows the hypothesized microphase separated structure. (b) Characteristic length scale of the microphase separation (left axis, closed squares) and mass fractal (left axis, closed triangles), as well as the peak sharpness (right axis, open squares) extracted from the model.

may reflect the broad dispersion of unstable modes for phase separation at short times.[46]

The best-fit model parameters are shown in Table 3. We note that the length scale associated with the fastest growing unstable mode, $2\pi\beta_{max}^{-1}$, is directly proportional to the characteristic size of the mass fractal (Fig. 4b), indicating self-similar growth of the internal structure of microdomains relative to their size as phase separation proceeds. Both quantities show an abrupt transition (over a temperature range of 0.2 °C) beginning at T_1 from nearly zero to saturated values on

Fig. 6 Cryo-TEM images of nanoemulsions under the following conditions: $\phi = 0.21$ vitrified at (a) 25 °C and (c) 45 °C; $\phi = 0.33$ vitrified at (b) 25 °C and (d) 45 °C. White arrows indicate droplet clusters. Red ellipses indicate pores.

droplets are small numbers of limited clusters with string-like morphology. It is possible that these clusters are merely coincidental, as the image represents the fluid microstructure at a single moment in time. However, in previous work, Kim *et al.* established that these nanoemulsions also form low-temperature viscoelastic phases due to the formation of temporary networks mediated by interdroplet bridging of polymer–surfactant complexes in solution.[26] Although it was found that the droplets remained colloidally stable in such cases, SANS measurements exhibited increased low-q scattering rather than a low-q plateau expected for well-dispersed droplets. Thus, the clusters apparent in cryo-TEM at low temperatures could be dynamic manifestations of this temporary network. More detailed studies of these clusters are peripheral to our primary aim, which is to test our hypotheses for the high-temperature gelation.

An image of the low-ϕ sample taken at 45 °C (between T_1 and T_2) exhibits a markedly different structure. Specifically, a network structure is observed, with alternating light and dark regions, which presumably correspond to the aqueous and oil phases, respectively. Individual droplets are not readily apparent in the image, possibly due to several reasons. First, potential scattering and attenuation of the transmitted electrons due to the dense network may produce artifacts which make identification of droplets difficult. Second, the effect of polymer bridging which is hypothesized to drive gelation[25] may result in a rather diffuse interface between droplets and the surrounding aqueous phase. Nevertheless, we find that the observed network structure is homogeneous across the entire sample above length scales corresponding to several droplets. This confirms the interpretation of the SANS/USANS data from the low-ϕ gel, in which the incipient gel is comprised of a homogeneous percolated network of fractal droplet clusters.

By contrast, images taken of the high-ϕ gel at 35 °C (Fig. 6d) exhibit network structure, but with significantly different characteristics. Firstly, the network is heterogeneous on length scales of hundreds of nanometers, apparent by large pore-like structures throughout the field of view. These structures appear as fairly uniform light regions, suggesting that they are nearly void of droplets. Secondly, there is significantly stronger image contrast between the dark (oil-rich) and light (water-rich) regions.

These results confirm that the low-q peak in USANS measurements on the high-ϕ gel arises due to strong structural heterogeneities, in this case reminiscent of microphase separation. The hypothesized structure (Fig. 5a, inset) consists of a bicontinuous network of droplet-rich and droplet-lean domains with a characteristic separation given by $1/\beta_{max}$. Due to both the fractal scattering above β_{max} in USANS and the relative contrast of the dense regions in the cryo-TEM image, we surmise that the droplet-rich domains are comprised of dense fractal aggregates of droplets.

Discussion

Homogeneous *versus* heterogeneous gelation

Our studies clearly indicate two different regimes, and associated kinetic pathways, of gelation in attractive nanoemulsions.

At sufficiently low volume fractions, gels exhibit homogeneous fractal network structure, with a concomitantly broad gel transition. From this, we hypothesize that T_1, at which both the fractal microstructure and increased elasticity appear, corresponds to the temperature at which interdroplet attractions[25] are sufficiently strong to produce transient droplet clusters, but not strong enough to induce a percolated microstructure. The fractal droplet clusters grow as the strength of attraction is increased above T_1. Finally, at T_2, the clusters are sufficiently large as to percolate the system, resulting in an arrested microstructure that is homogeneous above length scales corresponding to a few droplets. This behaviour is reminiscent of the dynamic percolation observed in dilute hard particle gels with short-range attractions,[40] in which gelation occurs entirely within the homogeneous fluid portion of the phase diagram.[7] Specifically, in the homogeneous fluid phase, dynamic formation and breakage of interparticle clusters results in a dynamic equilibrium distribution of cluster sizes. As the system is cooled, the equilibrium shifts to larger clusters, causing a significant increase in the fluid viscosity (corresponding to T_1). Eventually, the dynamic cluster size grows large enough to percolate the system, at which point a gel is formed (corresponding to T_2).

By contrast, the heterogeneous microstructure observed at sufficiently high volume fractions is clearly indicative of arrested phase separation, whereby a colloidal fluid quenched sufficiently into the fluid–fluid coexistence region will spontaneously separate into colloid-rich and colloid-poor regions. Arrest of this phase separation can occur in cases where a glass transition at high volume fraction (the so-called "attractive glass" state) bisects the gas–liquid binodal.[1] The hallmarks of arrested phase separation observed here include the strong low-q peak observed in USANS measurements. We associate this peak with long-wavelength density correlations consistent with simple models for off-critical phase separation,[46] and the rheologically observed gel temperature T_2 is remarkably consistent with the point at which these correlations are the sharpest.

To our knowledge, this is the first time both homogeneous percolation and arrested phase separation have been observed in the same system. In the case of our nanoemulsions, these mechanisms are clearly differentiated by the volume fraction of the colloid, although it is not clear at present whether the transition between homogeneous percolation and arrested phase separation is continuous or discontinuous. Nevertheless, it is interesting to note that the transition between the associated regimes of rheological scaling ($\phi \sim 0.23$) is close to the critical volume fraction for adhesive hard spheres ($\phi_c \sim 0.26$). We note that previous studies on systems above ϕ_c with short-range attractions[6,7] exhibit gelation by homogeneous percolation, whereas those with longer-range depletion attractions[11] exhibit gelation by arrested phase separation. Thus, the moderate range of attraction in our system ($\lambda/\langle D \rangle \sim 0.068$) may represent a regime where both conditions are observed. However, further studies are needed to determine whether non-equilibrium variables (such as the rate or depth of the temperature quench) are also important in determining whether homogeneous percolation or arrested phase separation provides the dominant mechanism for gelation.

Linear viscoelasticity

Our results establish that the mechanisms for gelation in attractively-driven nanoemulsion gels can be understood in terms of similar processes in hard particle colloidal gels. This explains the observed linear viscoelasticity through the gel transition for both the heterogeneous and homogeneous gels, including self-similar scaling of linear viscoelastic spectra at the gel point, and power-law scaling of the modulus and yield stress with droplet volume fraction.

Micromechanical theories for colloidal gels posit that viscoelasticity arises from a percolated network of aggregates with mass fractal dimension D, which are in turn made up of load-bearing particle chains having fractal dimension d.[48] Shih *et al.*[49] presented a simple model for dilute, homogeneous gels that relates the observed scaling exponents of the modulus and yield strain to the fractal dimensions d and D. The modulus and corresponding yield stress thus scale as

$$G_p \sim \phi^x; \quad x = \frac{3+d}{3-D} \qquad (3)$$

$$\sigma_y \sim \phi^z; \quad z = \frac{4+2d}{3-D}. \qquad (4)$$

The cluster fractal dimension D depends on the nature of the gelation kinetics, where $D \sim 1.7$ for diffusion-limited cluster aggregation (DLCA) and $D \sim 2.0$–2.2 for reaction-limited cluster aggregation (RLCA).[48,50] The chain fractal dimension d is then limited to $1 < d < D$. Given these definitions, typical values in the range $x = 2$–5 and $z = 5$–10 are observed.[48,49]

Interestingly, the power-law exponents we observe in the low-ϕ limit ($x \sim 17$ and $z \sim 20$) are significantly larger than those expected from given the value of $d \sim 2.3$ from our USANS measurements (or any physical values of same). The large exponents could be due to the complex nature of our nanoemulsions. For example, polymer–droplet interactions may contribute significantly to the viscoelasticity of the aggregated droplet network,[26] and such contributions would be exacerbated at low ϕ due to reduced droplet–droplet interactions within the percolated droplet network. Nevertheless, the precise origin of these anomalously large exponents warrants further study beyond the scope of this work.

By contrast, the exponents observed for high-ϕ heterogeneous gels ($x \sim 3$ and $z \sim 5$) are within the expected range for DLCA gels. This is counter-intuitive, since these relationships were originally formulated to explain data for homogeneous gels.[49] This suggests that the structural parameters in eqn (3) and (4) correspond to the granular fractal structure of the gel at length scales above the characteristic cluster size (ξ_m), and not the internal distribution of droplet–droplet contacts within clusters. This could explain why gels presumably formed by arrested phase separation would have viscoelasticity that scales similar to those formed by percolation, provided that the cluster–cluster correlations (*i.e.* the low-q peak in the scattering data) grow self-similarly during the gelation process as suggested by some theories.[51] We note that this hypothesis is in contrast with recent results on dilute depletion-induced particulate gels,[17] which suggested that viscoelasticity is predominately determined by the local bond number distribution of particles within clusters, and not the larger cluster–cluster scale structure.

Non-linear viscoelasticity

Our combined rheological and microstructural studies provide new insight into the nature of various yielding processes in colloidal gels. Specifically, we note that the homogeneous gels formed at $\phi < 0.23$ exhibit a single, distinct yield point, whereas the heterogeneous gels with $\phi > 0.23$ exhibit so-called "two-step" yielding observed in other gelling systems at moderate volume fraction.[21,33] This suggests that the origin of two-step yielding might arise from large-scale structural heterogeneity (in this case due to arrested phase separation), since a heterogeneous distribution of cluster–cluster bonds should give rise to a broad distribution of microscopic yielding processes. This is a potential alternative to recently proposed hypotheses,[21,23,24,52] which posit that two-step yielding results from a combination of two distinct microstructural processes: bond rupture and cage breakage, which both occur at local length scales on the order of single particles and their nearest neighbours, and do not require a heterogeneous structure.

Conclusions

We have demonstrated, in a model thermoreversible nanoemulsion system with moderate-range attractions, that colloidal gelation can proceed either due to homogeneous percolation or arrested phase separation depending on the volume fraction of the suspension. For ϕ sufficiently smaller than 0.23, gelation is caused by growth and subsequent percolation of fractal clusters, which begins at the onset of colloidal instability (T_1) and becomes arrested at the macroscopic gel point (T_2). For ϕ sufficiently larger than 0.23, gelation is caused by arrested phase separation, signified by the development of strong cluster–cluster correlations. These correlations are sharpest at the gel point, are well-described by the Cahn–Hilliard model, and become arrested abruptly as the system is quenched above T_2. The transition between these two regimes of gelation coincides closely with the gas–liquid critical point for adhesive hard spheres.

This is contrary to recent hypotheses,[6,7] which posit that gelation occurs universally by homogeneous percolation *vis-à-vis* the extended law of corresponding states,[53] and suggests that the gelation mechanism is in fact highly sensitive to the details of the interparticle potential. Our results call for more detailed experimental and theoretical studies, where the dependence of the gelation mechanism on both the range of the interparticle potential and the kinetic path taken to the gelled state can be explored. For example, previous theoretical simulations on colloidal fluids with short-range attraction and long-range repulsion showed the existence of two arrested phases, one occurring at relatively low volume fraction consisting of a glassy suspension of clusters, and another occurring at high volume fraction consisting of a percolated network.[54] This is reminiscent of the situation found here, and warrants further experiments where the dynamics (rather than the static

structure) of the various gel phases are measured and compared with these simulations. Likewise, our experiments call for new simulations where the structural dynamics at length scales much larger than the primary particle size can be observed.

Finally, the significant qualitative differences in yielding between the two different types of gels suggests that a distribution of yielding processes due to large-scale heterogeneity (in the case of high volume fraction gels) may play a significant role in the occurrence of two-step yielding which has been previously overlooked. Ongoing studies are aimed at testing this idea by performing *in situ* SANS/USANS measurements during yielding in order to better relate changes in large-scale microstructure to the observed nonlinear rheological behaviour.

Experimental

Nanoemulsion preparation

Silicone oil (viscosity 5 cSt at 25 °C), sodium dodecyl sulphate (SDS, >99%), and polyethylene glycol diacrylate (PEGDA, $M_n = 700$ g mol^{-1}) were obtained from Sigma Aldrich and used without further purification. Aqueous solutions were prepared in 18.3 MΩ deionized water. Deuterium oxide (D$_2$O, 99.9%, Cambridge Isotope Laboratories) was used in the solvent for SANS/USANS measurements to enhance neutron contrast.

Nanoemulsions were prepared according to a procedure published elsewhere[25] using an Avestin Emulsiflex-C3 high-pressure homogenizer. Briefly, a crude pre-emulsion is prepared by adding silicone oil dropwise to the continuous phase while stirring until the desired oil volume fraction is reached. The pre-emulsion is then homogenized for a number of passes at a constant homogenizing pressure. The size distribution of the resulting nanoemulsion droplets is then obtained by dynamic light scattering (DLS) using a Brookhaven Instruments BI-200SM instrument with a 514 nm Argon ion laser. Nanoemulsion samples were prepared by diluting the mother nanoemulsion to 0.2 vol% with the continuous phase in the absence of surfactant. Intensity autocorrelation functions were measured at 90° and analysed using a cumulant analysis to obtain the average hydrodynamic diameter, $<D>$, and polydispersity, σ.

To obtain the nanoemulsions with a series of droplet volume fraction, ϕ, used in this work, a mother emulsion containing $\phi = 0.33$ silicone oil dispersed in an aqueous phase containing 33 vol% PEGDA and 200 mM SDS in a solvent of 82/18 v/v H$_2$O/ D$_2$O was prepared by homogenizing at 15 kpsi for 21 passes, resulting in a nanoemulsion with $<D> = 36$ nm and $\sigma/<D> = 0.213$. The mother emulsion was then diluted with a 33 vol% solution of PEGDA in 82/18 H$_2$O/D$_2$O to achieve samples with the desired droplet volume fraction. We note that dilution of silicone oil-in-water nanoemulsions with their own continuous phase in the absence of surfactant has a negligible effect on the droplet size distribution.[25,55]

Rheological characterization

Rheological measurements were carried out using a TA Instruments ARG2 stress-controlled rheometer with a 60 mm, 2° aluminium upper cone geometry and a temperature-controlled lower Peltier plate geometry. A solvent trap wetted with the H$_2$O/ D$_2$O solvent was used in order to prevent appreciable sample evaporation. All samples were loaded at 25 °C and subjected to a pre-shear of 20 s^{-1} for 60 s in order to ensure uniform, reproducible measurements.

After loading, the thermal gelation behaviour of the nanoemulsions was characterized using small-amplitude oscillatory strain at a fixed frequency of $\omega = 10$ rad s^{-1} and strain amplitude of $\gamma_0 = 0.05\%$ (chosen to ensure measurements in the linear viscoelastic regime) during a temperature ramp of 0.5 °C min^{-1} from 25 °C to 65 °C, or until the observed change in moduli with increasing temperature was less than 2% per °C. Upon the completion of the temperature ramp and frequency sweep measurements, the non-linear viscoelasticity of samples exhibiting gelation were probed using large amplitude oscillatory shear (LAOS). LAOS measurements were performed using stress amplitude sweeps at a frequency of 10 rad s^{-1}. Forward sweeps were performed to examine yielding of the nanoemulsion sweeps. Subsequent backward sweeps showed significant unrecoverable hysteresis, suggesting that yielding is irreversible above the gelation temperature. However, we note that previous studies show that the nanoemulsion can be rejuvenated by quenching below the gel temperature.[25]

For all samples, frequency sweeps at a strain of $\gamma_0 = 0.05\%$ were performed at both the lowest and highest temperatures of the temperature ramp to obtain linear viscoelastic spectra of both the liquid and gelled material. These frequency sweeps were performed for both increasing and decreasing frequencies, and in all cases no significant hysteresis was observed. For select samples, additional frequency sweep measurements were made at various temperatures spanning the temperature ramp to examine the temperature-dependence of the linear viscoelastic spectra.

Small and ultra-small angle neutron scattering

Small angle neutron scattering (SANS) and ultra-small angle neutron scattering (USANS) were carried out at the NIST Center for Neutron Research (Gaithersburg, MD). SANS was performed on the NG7 30 m SANS instrument.[56] SANS data were collected using neutrons with a wavelength of $\lambda = 6$ Å and $\Delta\lambda/\lambda = 0.11$ at detector distances of 1 m, 4 m, and 13.5 m, and with a wavelength of $\lambda = 8.4$ Å and $\Delta\lambda/\lambda = 0.11$ at a detector distance of 15.3 m. Samples were loaded into 1 mm thick titanium scattering cells with transparent quartz windows and placed in the 10CB sample environment, whose temperature was controlled using a Julabo temperature-controlled bath.

USANS was performed on the BT5 perfect crystal diffractometer.[57,58] Samples were loaded into scattering cells and placed in the 6CB sample environment, whose temperature was also controlled using a Julabo temperature-controlled bath. Data were reduced and (where necessary) de-smeared using the National Institute of Standards and Technology IGOR software package.[58]

Due to the fine temperature control requirements for SANS and USANS experiments, a reference cell filled with D$_2$O was

placed in the 10 CB chamber and monitored to obtain the most accurate measurements of the sample temperature. This allowed for adequate temperature control with $\pm 0.05\ ^{\circ}$C precision. All samples were allowed to equilibrate for at least 30 min. Extreme care was taken to make sure the reference cell was equilibrated at the desired temperature before measurement.

Cryo-transmission electron microscopy

Cryo-transmission electron microscopy (cryo-TEM) measurements were performed on nanoemulsions containing $\phi = 0.21$ and $\phi = 0.33$ at three different temperatures (25, 35 and 45 $^{\circ}$C) using a Controlled Environmental Vitrification System (CEVS). The vitrification chamber was set at the desired temperature and 100% humidity to avoid sample evaporation artifacts. Nanoemulsion samples were liquid when at 25 $^{\circ}$C and 35 $^{\circ}$C at $\phi = 0.21$ and 25 $^{\circ}$C at $\phi = 0.33$. On a lacey carbon grid (Ted Pella, Inc), 3 μl of polymeric solution was deposited using micro pipette. The sample was deposited on the grid within the vitrification system, preventing water evaporation and temperature changes in the sample. Excess volume of the sample was removed by a blotting step, absorbing the excess sample by filter paper to form thin films of liquid spanning the grid holes. For temperatures near or above the gel point, TEM specimens were prepared at low temperatures in the liquid state, and then solidified by increasing the temperature after blotting. The sample-bearing grid was then plunged into a liquid ethane reservoir, close to its freezing point. Contact with the cryogen vitrifies the sample and preserves all of the microstructures in their native hydrated states. The specimen was transferred under liquid nitrogen to the cooled tip of a cryo transfer stage (Gatan 626 DH). Finally, the stage was inserted under positive dry nitrogen pressure into a JEOL 2100 TEM and imaged at slight under-focus.

Acknowledgements

Notes and references

1 E. Zaccarelli, *J. Phys.: Condens. Matter*, 2007, **19**, 323101.

2 R. Mezzenga and P. Fischer, *Rep. Prog. Phys.*, 2013, **76**, 046601.

3 M. N. Lee and A. Mohraz, *J. Am. Chem. Soc.*, 2011, **133**, 6945–6947.

4 J. C. Conrad, S. R. Ferreira, J. Yoshikawa, R. F. Shepherd, B. Y. Ahn and J. A. Lewis, *Curr. Opin. Colloid Interface Sci.*, 2011, **16**, 71–79.

5 D. Frenkel, *Science*, 2002, **296**, 65–66.

6 A. P. R. Eberle, R. Castaneda-Priego, J. M. Kim and N. J. Wagner, *Langmuir*, 2012, **28**, 1866–1878.

7 A. P. R. Eberle, N. J. Wagner and R. Castaneda-Priego, *Phys. Rev. Lett.*, 2011, **106**, 105704.

8 Y. C. Chiew and E. D. Glandt, *J. Phys. A: Math. Gen.*, 1983, **16**, 2599–2608.

9 P. J. Lu, E. Zaccarelli, F. Ciulla, A. B. Schofield, F. Sciortino and D. A. Weitz, *Nature*, 2008, **453**, 499–503.

10 M. A. Miller and D. Frenkel, *J. Chem. Phys.*, 2004, **121**, 535–545.

11 M. Laurati, G. Petekidis, N. Koumakis, F. Cardinaux, A. B. Schofield, J. M. Brader, M. Fuchs and S. U. Egelhaaf, *J. Chem. Phys.*, 2009, **130**, 134907.

12 S. Manley, H. M. Wyss, K. Miyazaki, J. C. Conrad, V. Trappe, L. J. Kaufman, D. R. Reichman and D. A. Weitz, *Phys. Rev. Lett.*, 2005, **95**, 238302.

13 F. Cardinaux, T. Gibaud, A. Stradner and P. Schurtenberger, *Phys. Rev. Lett.*, 2007, **99**, 118301.

14 J. C. Conrad, H. M. Wyss, V. Trappe, S. Manley, K. Miyazaki, L. J. Kaufman, A. B. Schofield, D. R. Reichman and D. A. Weitz, *J. Rheol.*, 2010, **54**, 421–438.

15 E. Zaccarelli and W. C. Poon, *Proc. Natl. Acad. Sci. U. S. A.*, 2009, **106**, 15203–15208.

16 M. A. Miller and D. Frenkel, *Phys. Rev. Lett.*, 2003, **90**, 135702.

17 J. Vermant and M. J. Solomon, *J. Phys.: Condens. Matter*, 2005, **17**, R187–R216.

18 T. Gibaud, D. Frelat and S. Manneville, *Soft Matter*, 2010, **6**, 3482–3488.

19 F. Pignon, A. Magnin, J.-M. Piau, B. Cabane, P. Lindner and O. Diat, *Phys. Rev. E: Stat. Phys., Plasmas, Fluids, Relat. Interdiscip. Top.*, 1997, **56**, 3281.

20 N. Koumakis, M. Laurati, S. Egelhaaf, J. Brady and G. Petekidis, *Phys. Rev. Lett.*, 2012, **108**, 098303.

21 N. Koumakis and G. Petekidis, *Soft Matter*, 2011, **7**, 2456–2470.

22 M. Laurati, S. Egelhaaf and G. Petekidis, *J. Rheol.*, 2011, **55**, 673.

23 Z. Shao, A. S. Negi and C. O. Osuji, *Soft Matter*, 2013, **9**(22), 5492–5500.

24 H. K. Chan and A. Mohraz, *Phys. Rev. E: Stat., Nonlinear, Soft Matter Phys.*, 2012, **85**, 041403.

25 M. E. Helgeson, S. E. Moran, H. Z. An and P. S. Doyle, *Nat. Mater.*, 2012, **11**, 344–352.

26 J. Kim, Y. X. Gao, C. Hebebrand, E. Peirtsegaele and M. E. Helgeson, *Soft Matter*, 2013, **9**, 6897–6910.

27 J. N. Wilking, C. B. Chang, M. M. Fryd, L. Porcar and T. G. Mason, *Langmuir*, 2011, **27**, 5204–5210.

28 J. E. Martin, J. Wilcoxon and J. Odinek, *Phys. Rev. A: At., Mol., Opt. Phys.*, 1991, **43**, 858–872.

29 M. Kluppel and G. Heinrich, *Rubber Chem. Technol.*, 1995, **68**, 623–651.

30 H. H. Winter and F. Chambon, *J. Rheol.*, 1986, **30**, 367–382.

31 V. Prasad, V. Trappe, A. D. Dinsmore, P. N. Segre, L. Cipelletti and D. A. Weitz, *Faraday Discuss.*, 2003, **123**, 1–12.

32 G. Foffi, K. A. Dawson, S. V. Buldyrev, F. Sciortino, E. Zaccarelli and P. Tartaglia, *Phys. Rev. E: Stat., Nonlinear, Soft Matter Phys.*, 2002, **65**, 050802.

33 M. Laurati, S. U. Egelhaaf and G. Petekidis, *J. Rheol.*, 2011, **55**, 673–706.

34 H. Guo, S. Ramakrishnan, J. L. Harden and R. L. Leheny, *J. Chem. Phys.*, 2011, **135**, 154903.

35 B. Chung, S. Ramakrishnan, R. Bandyopadhyay, D. Liang, C. F. Zukoski, J. L. Harden and R. L. Leheny, *Phys. Rev. Lett.*, 2006, **96**, 228301.

36 L. Cipelletti, S. Manley, R. C. Ball and D. A. Weitz, *Phys. Rev. Lett.*, 2000, **84**, 2275–2278.

37 A. Duri and L. Cipelletti, *Europhys. Lett.*, 2006, **76**, 972–978.

38 P. Varadan and M. J. Solomon, *Langmuir*, 2003, **19**, 509–512.

39 A. E. Bailey, W. C. K. Poon, R. J. Christianson, A. B. Schofield, U. Gasser, V. Prasad, S. Manley, P. N. Segre, L. Cipelletti, W. V. Meyer, M. P. Doherty, S. Sankaran, A. L. Jankovsky, W. L. Shiley, J. P. Bowen, J. C. Eggers, C. Kurta, T. Lorik, P. N. Pusey and D. A. Weitz, *Phys. Rev. Lett.*, 2007, **99**, 205701.

40 H. Wu, J. J. Xie, M. Lattuada and M. Morbidelli, *Langmuir*, 2005, **21**, 3291–3295.

41 J. Teixeira, *J. Appl. Crystallogr.*, 1988, **21**, 781–785.

42 S. Sinha, *Phys. D*, 1989, **38**, 310–314.

43 P. Z. Wong and Q. Z. Cao, *Phys. Rev. B: Condens. Matter Mater. Phys.*, 1992, **45**, 7627–7632.

44 R. M. Baram and H. J. Herrmann, *Fractals*, 2004, **12**, 293–301.

45 D. Aarts and H. Lekkerkerker, *J. Phys.: Condens. Matter*, 2004, **16**, S4231.

46 J. C. Li and D. K. Ross, *J. Phys.: Condens. Matter*, 1994, **6**, 351–362.

47 S. Sinha, T. Freltoft and J. Kjems, *Kinet. Aggregation Gelation*, 1984, **19842**, 87–90.

48 C. J. Rueb and C. F. Zukoski, *J. Rheol.*, 1997, **41**, 197–218.

49 W.-H. Shih, W. Y. Shih, S.-I. Kim, J. Liu and I. A. Aksay, *Phys. Rev. A: At., Mol., Opt. Phys.*, 1990, **42**, 4772.

50 J. A. Yanez, E. Laarz and L. Bergström, *J. Colloid Interface Sci.*, 1999, **209**, 162–172.

51 H. Furukawa, *Phys. A*, 1984, **123**, 497–515.

52 B. Rajaram and A. Mohraz, *Phys. Rev. E: Stat., Nonlinear, Soft Matter Phys.*, 2011, **84**, 011405.

53 M. G. Noro and D. Frenkel, *J. Chem. Phys.*, 2000, **113**, 2941–2944.

54 J. C. F. Toledano, F. Sciortino and E. Zaccarelli, *Soft Matter*, 2009, **5**, 2390–2398.

55 K. Meleson, S. Graves and T. G. Mason, *Soft Matter*, 2004, **2**, 109–123.

56 C. Glinka, J. Barker, B. Hammouda, S. Krueger, J. Moyer and W. Orts, *J. Appl. Crystallogr.*, 1998, **31**, 430–445.

57 J. Barker, C. Glinka, J. Moyer, M. Kim, A. Drews and M. Agamalian, *J. Appl. Crystallogr.*, 2005, **38**, 1004–1011.

58 S. R. Kline, *J. Appl. Crystallogr.*, 2006, **39**, 895–900.